

# Experimental and Theoretical Examination of the Kinetic Isotope Effect in Cytochrome P450 Decarboxylase OleT

Matthew Dutra,<sup>†</sup> Jose A. Amaya,<sup>†</sup> Shannon McElhenney,<sup>†</sup> Olivia M. Manley,<sup>‡</sup>  
Thomas M. Makris,<sup>\*,‡</sup> Vitaly Rassolov,<sup>†</sup> and Sophya Garashchuk<sup>\*,†</sup>

<sup>†</sup>*Department of Chemistry & Biochemistry, University of South Carolina, Columbia, South  
Carolina 29208*

<sup>‡</sup>*Molecular and Structural Biochemistry, North Carolina State University, Raleigh, North  
Carolina 27695*

E-mail: tmmakris@ncsu.edu; garashchuk@sc.edu

## Abstract

Using a combination of experimental studies, theory, simulation and modeling, we investigate the hydrogen atom transfer (HAT) reaction by the high-valent ferryl cytochrome P450 (CYP) intermediate known as Compound I, a species that is central to innumerable and important detoxification and biosynthetic reactions. The P450 decarboxylase known as OleT converts fatty acids, a sustainable biological feedstock, into terminal alkenes, and thus is of high interest as a potential means to produce fungible biofuels. Previous experimental work has established the intermediacy of Compound I in the C-C scission reaction catalyzed by OleT and an unprecedented ability to monitor the HAT process in the presence of bound fatty acid substrates. Here, we leverage the kinetic simplicity of the OleT system to measure the activation barriers for CYP HAT

and the temperature dependence of the substrate  $^2\text{H}$  kinetic isotope effect. Notably, neither measurement has been previously accessible for a CYP to date. Theoretical analysis alludes to the significance of substrate fatty acid coordination for generating the hydrogen donor/acceptor configurations that are most conducive for HAT to occur. The analysis of the two-dimensional potential energy surface, based on multireference electronic wavefunctions, illustrates the uncoupled character of the hydrogen motion. Quantum dynamics calculations along the hydrogen reaction path demonstrate that hydrogen tunneling is essential to qualitatively capture the experimental isotope effect, its temperature dependence, and appropriate activation energies. Overall, a more fundamental understanding of the OleT reaction coordinate contributes to the development of biomimetic catalysts for controlled C-H bond activation, an outstanding current challenge for (bio)synthetic chemistry.

## 1 Introduction

Understanding the mechanisms for controlled C-H bond activation is an outstanding challenge for synthetic chemistry. Enzymatic systems often serve as a template for the “bio-inspired” design of small molecule catalysts, with cytochrome P450s (CYPs) assuming a central role due to their ability to perform efficient hydrogen atom transfer (HAT) on extremely challenging substrates. Despite over a half-century of intensive study, a number of fundamental questions remain regarding the mechanism for CYP-catalyzed HAT, and in particular, the oxidative proficiency of the central ferryl intermediate - an Fe(IV)-oxo  $\pi$ -cation radical species known as Compound I (CYP-I)<sup>1</sup> in this process.

The  $\text{H}_2\text{O}_2$  dependent decarboxylases known as OleT convert  $C_n$  chain length fatty acids to  $C_{n-1}$  terminal alkenes and  $\text{CO}_2$  using CYP-I as an oxidant to initiate the C-C cleavage process. A current mechanism for the overall catalytic cycle, based principally on transient absorption studies, is shown in Fig. 1. As some of us have shown using stopped-flow methods, OleT serves as an excellent means with which to generate appreciable levels of

CYP-I and to interrogate its reactivity.<sup>2,3</sup> Although a good deal of our (and others') focus has centered on the identification of factors that enable the enzyme to circumvent more canonical oxygen-rebound chemistry that typifies most CYPs and was initially posited by Groves,<sup>4</sup> our efforts here strictly examine the HAT step catalyzed by CYP-I. Notably, extremely efficient substrate-triggered H<sub>2</sub>O<sub>2</sub> activation in OleT enzymes allows one to monitor the kinetics for CYP-I in its reaction with bound fatty acid substrates.<sup>2,3</sup> This approach ensures that the apparent rates for CYP-I decay are largely unobscured from preceding kinetic processes, namely the substrate associative steps that hinder measurements of CYP-I reactivity in O<sub>2</sub>-activating CYPs.

In the current study, we utilize a hybrid experimental and theoretical approach to better understand CYP HAT. The kinetic simplicity of the OleT system is leveraged to measure the activation thermodynamics of CYP-I, providing direct metrics for C-H bond activation barriers and the temperature dependence of the <sup>2</sup>H KIE. To the best of our knowledge, this represents the first time these parameters have been accessible for a ferryl intermediate in a CYP, and more globally, any mononuclear Fe<sup>4+</sup>-oxo system to date. Using these parameters as a guide for computation, the HAT step is further examined using electronic structure (ES) theory and quantum dynamics for both one- and two-dimensional reaction path models developed within a truncated molecular representation of the active site. The full model describes the correlated motions of the two hydrogens bound to the donor carbon of the substrate with an acceptor oxygen attached to the enzymatic iron center; these motions collectively define two coordinates for a potential energy surface (PES) interpolated from multireference calculations. The one-dimensional models are taken as slices of this PES.

This reduced representation of the HAT reaction, which according to our experiments partially proceeds via tunneling, is justified by the timescale separation of the protein motions (nanoseconds for the sidechains) and the electron/proton/hydrogen/hydride transfer (0.1-1 picoseconds). In other words, the HAT in the active site happens sufficiently fast for the larger molecular environment to be treated as space-fixed. A hierarchy of timescale

separation in dynamics in relation to enzyme catalysis has been discussed, for example, in Refs.<sup>5-8</sup> Furthermore, electronic structure studies of a truncated enzyme center, fully optimized either in gas phase or within an implicit solvent, are shown to be a proven alternative to QM/MM models (e.g. Refs<sup>4</sup> and<sup>9</sup>). Additional rationale for using a truncated space-fixed active site (in our case of  $\sim 60$  atoms) is provided by the demands of accurate nuclear quantum dynamics calculations, especially in the tunneling regime, which call for a high-quality PES based on DFT or correlated *ab initio* methods. Thus, as elaborated elsewhere,<sup>10</sup> we bypass large-scale simulations of a fully represented enzyme and its environment and instead construct the HAT-conducive configuration of a truncated active site based on the crystal structure of the apoenzyme (with a fairly rigid heme center) and fatty acid substrate. According to QM/MM calculations on OleT in Ref.,<sup>11</sup> ‘no dramatic changes in geometry, spin-state ordering and relative energies were obtained’ upon testing two QM regions and several basis sets, which is consistent with earlier conclusions for analogous enzymes; QM/MM calculations by Harvey and co-workers<sup>12</sup> on similar CYP450 models with partial inclusion of the salt bridges have also shown no significant impact on the enzymatic structure.

We also note that molecular cluster models are useful for less conventional quantum dynamics studies of large systems, in which the impact of nuclear quantum effects on chemical reactivity<sup>7,13,14</sup> can be elucidated. In addition, these small models can be readily adapted to new systems in conjunction with experiments.<sup>8</sup> Furthermore, recent developments such as the rate constant expressions for the proton-coupled electron transfer reactions for the KIE in lipoyxygenase,<sup>15</sup> a qualitative quantum rate model for hydrogen atom transfer (HAT) in soybean lipoyxygenase,<sup>16</sup> and a measured KIE used as ‘evidence for a Marcus-like model of hydride tunneling’<sup>17</sup> serve to highlight the role these various theoretical approaches can play to give insight into processes in extended molecular systems alongside state-of-the-art large-scale atomistic simulations. Thus, we argue that when it comes to nuclear quantum effects and HAT KIE, the approach pursued in this work – a low-dimensional dynamics study of

HAT based on *ab initio* electronic structure calculations of a ‘minimal’ OleT representation calibrated by experiment – achieves a reasonable balance between accuracy and feasibility.

The remainder of this paper is organized as follows: Section 2 describes the experimental methods and results, Section 3.1 describes the molecular models and theoretical methods employed to analyze the OleT system, and Section 3.2 presents the results and analysis of the quantum dynamics. Conclusions and outlook are given in Section 4.

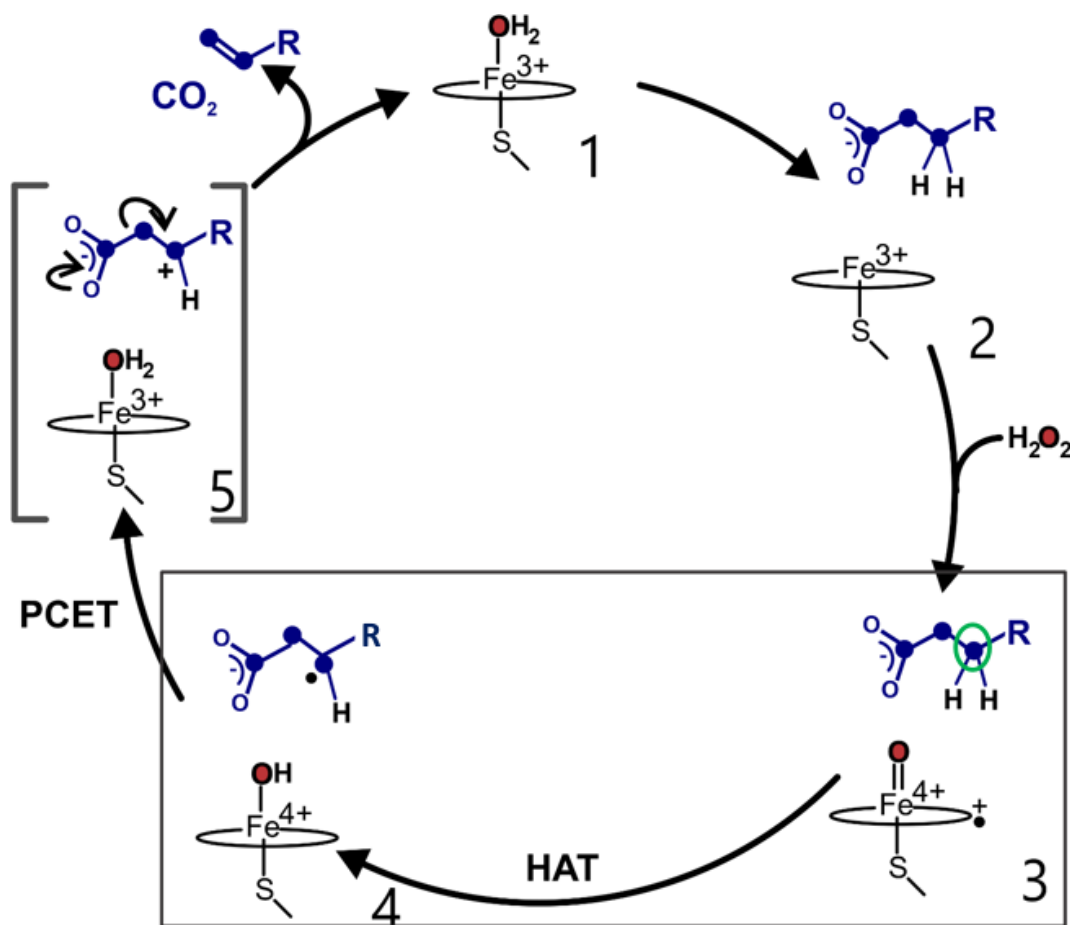


Figure 1: Mechanism for OleT decarboxylation as revealed by transient kinetics studies. The hydrogen atom transfer (HAT) step that is the focus of this study, is highlighted. The overall mechanism proceeds by fatty acid binding to the low-spin enzyme (1) and results in transition to the high-spin form (2). Compound I (3) is generated following  $\text{H}_2\text{O}_2$  activation and performs C3-H cleavage to form the oxyferryl species Compound II (4). Decarboxylation is thought to proceed by further oxidation of the substrate, coupled to recruitment of a proton, to regenerate the low-spin aquo-ferric resting state.

## 2 Experimental

Stopped-flow experiments were performed on an Applied Photophysics Ltd. SX20 stopped-flow spectrophotometer. The recombinant expression and purification of OleT from *Staphylococcus aureus* (OleT<sub>SA</sub>) has been reported previously.<sup>18</sup> Eicosanoic acid (either protiated or perdeuterated) bound OleT was rapidly mixed with 500 molar equivalents of H<sub>2</sub>O<sub>2</sub>. To monitor the reaction with deuterated substrate, 5  $\mu$ M OleT (post-mix concentration) was used. For monitoring faster reactions with protiated substrates, 15  $\mu$ M OleT was used to maximize the amplitude of the CYP-I intermediate for adequate fitting. All solutions were prepared in 200 mM potassium phosphate buffer at pH 7.5.

Data was collected by a photodiode array (PDA) for full spectral analysis or via a photomultiplier tube (PMT) for rate-constant determination. Data was collected at temperatures ranging from 4 to 21 °C. The methods for determining rate constants for CYP-I decay were described previously.<sup>3</sup> Briefly, the kinetics of OleT Compound I decay was monitored at 690 nm; Compound I is the only intermediate in the single turnover reaction sequence with an appreciable absorption at this wavelength, facilitating analysis. The time-course at 690 nm was adequately fit to a single exponential decay expression using ProData viewer software.

Fitting the Arrhenius plots ( $\ln(k)$  vs.  $1/T$ ) provides the activation energy ( $E_a$ ) from the slope which is determined from the negative slope of the plot multiplied by the ideal gas constant ( $R$ ). Linear fitting of the Eyring plot (dependence of  $\ln(k/T)$  on  $1/T$ ) provides  $\Delta H^\ddagger$ , which is the negative slope of the Eyring plot multiplied by the gas constant ( $R$ ).  $\Delta S^\ddagger$  is determined from intercept of the plot, which under the no-recrossing assumption of the transition state theory is equal to  $23.76 + \Delta S^\ddagger/R$  in J/mol.

Representative timecourses for the reaction of OleT Compound I with eicosanoic acid at temperatures ranging from 4 to 20 °C are shown in Fig. 2A. The resulting Arrhenius plots for the protiated substrate and a perdeuterated isotopologue are shown in Fig. 2B and reveal a <sup>2</sup>H KIE  $\sim$  15 at 4 °C. This value is slightly higher than that previously measured for another OleT ortholog and may reflect either some variability between enzymes or a faster H<sub>2</sub>O<sub>2</sub>

activation step that leads to Compound I. Nonetheless, the linear nature of the plot suggests that there is no apparent change in mechanism within this temperature regime. The resulting  $\Delta H$ ,  $\Delta S$  and  $E_a$  values derived from Eyring plots for the decay reactions are provided in Table 1. Several interesting features result from this analysis. First, the measured activation barrier for the reaction of CYP-I measured here is much smaller than those estimated from many previous theoretical studies that typically predict activation barriers on the order of  $\sim 20$  kcal/mol.<sup>11</sup> Instead, the  $E_a$  for OleT HAT closely resembles that recently estimated by Green ( $\sim 6$  kcal/mol) obtained from a combined experimental/theoretical study.<sup>19</sup> The difference in  $E_a$  values between the protiated and deuterated substrate ( $E_a(\text{H})-E_a(\text{D}) \sim 5$  kcal/mol) exceeds the difference in zero-point energy (ZPE) for the two substrates ( $\Delta\text{ZPE} \sim 2$  kcal/mol). Taken together with the pre-exponential factor ratio of  $A_H/A_D = 1.54 > 1$ , OleT has all of the requisite hallmarks that suggest that HAT proceeds via some degree of hydrogen-atom tunneling,<sup>9,20</sup> investigated in detail below.

Table 1: Activation thermodynamics data obtained from linear fits of the rate measurements, as described in-text.

	Protiated		Deuterated	
	kJ/mol	kcal/mol	kJ/mol	kcal/mol
$\Delta H$	14.14	3.380	36.48	8.719
$\Delta S$	-0.1443	$3.449 \times 10^{-2}$	$-8.602 \times 10^{-2}$	$2.056 \times 10^{-2}$
$E_a$	16.52	3.948	38.85	9.285

### 3 Theoretical analysis and discussion

In this section, first we describe one- and two-dimensional models of HAT, that are based on available experimental geometry and developed to approximate the experimental activation energies. Then quantum dynamics is employed to assess the temperature-dependence of the kinetic isotope effect.

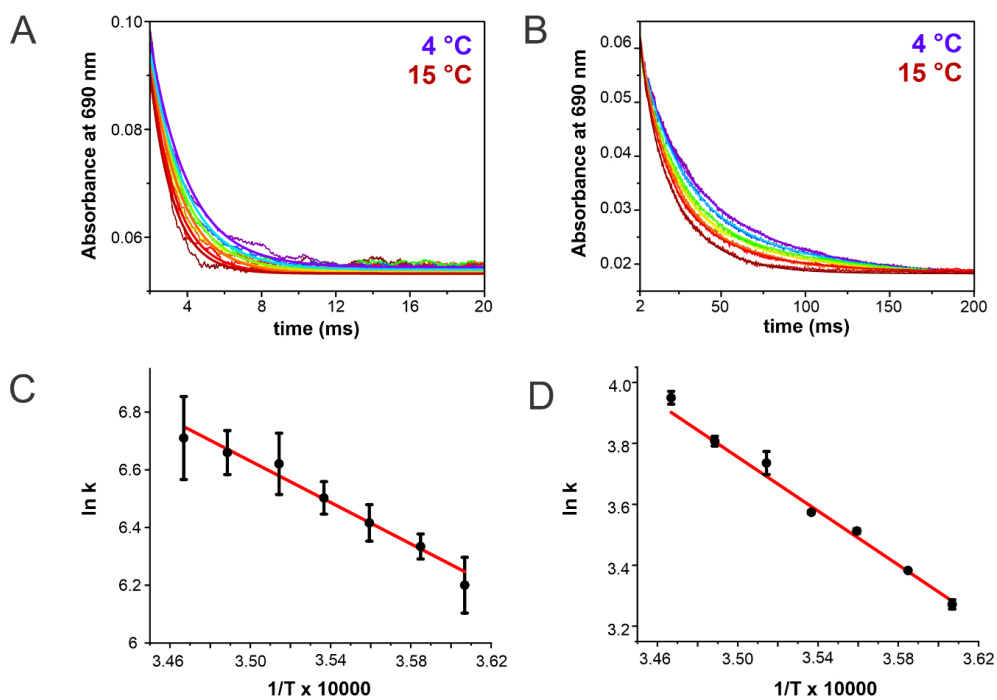


Figure 2: Representative time course for the decay of Compound I as monitored at 690 nm for protiated (A) and perdeuterated (B) eicosanoic acid. The observed rate constants were used to generate the corresponding Arrhenius plots that are shown in (C) and (D) respectively.

### 3.1 Electronic structure and the reaction path models

Theoretical studies of CYP450 enzymes have been extensive (see review<sup>21</sup> for details). One observation of particular relevance to our system is the “push effect” by various axial ligands on the formation of key intermediates in the catalytic cycle. Indeed, the chemical properties of this axial ligand have been correlated to both the length of the iron-oxo bond and overall activation energy for the transfer step of the hydrogen abstraction process, emphasizing its apparent importance within the enzymatic complex. When it comes to the electronic structure (ES) of the CYP450 family, the collective conclusion from prior work is that at the single-reference DFT level of the ES, the high and low spin states are generally close in energy, and the low spin-state computed within unrestricted Kohn-Sham orbitals shows significant mixed-spin character. Therefore, we have carefully developed a molecular model for the OleT system, which reasonably represents the experimental system and is sufficiently small (< 100 atoms), so that the HAT process can be investigated via a multireference ES method along a two-dimensional reaction path. The ES calculations are performed with the QChem-5.3<sup>22</sup> package visualized in IQmol,<sup>23</sup> and with Spartan18.<sup>24</sup> MAPLE<sup>25</sup> is used in analytic work. The multireference calculations are performed using GAMESS (v. June 30, 2019)<sup>26</sup> using XSEDE computational facilities.<sup>27</sup>

The apo-enzyme model – ultimately reduced to the porphyrin ring and -S-CH<sub>3</sub> ligand (Fig. S11) – and its DFT-based analysis are described in Ref.<sup>10</sup> To reconstruct the active state enzyme, crystal structures for the apo-state enzyme, the post-reaction fatty acid, and the molecular surroundings are used. Compounds I/II are created by adding O/OH to the model apoenzyme with the -SCH<sub>3</sub> ligand; the positions of the heavy atoms are taken from the experimental geometry. The ES is computed at the B3LYP-D3 level using 6-31G\* and 6-31+G\*\* basis sets, optimizing the positions of the O/OH atoms in each case. The low- and high-spin energies and frequencies are summarized in Table 2. The energies are given with respect to the energy of the low-spin Cpd I species, and the energy of hydrogen abstraction,  $\Delta = E_{\text{CH}_4} - E_{\text{CH}_3}$ , is subtracted from the Cpd II energies. For reference, B3LYP/6-31G\*

calculations using the full thiolate ligand are also displayed. These results show that the low- and high-spin states of Cpd I are nearly degenerate in energy (the low-spin state is favored by 2-3 kJ/mol (0.5-0.7 kcal/mol)), and the Fe=O bond in the high-spin state is elongated by  $\sim 0.05$  Å with a lower force constant. For Cpd II, the low- and high-spin states are characterized by further stretching of the Fe-O bond to  $\sim 1.82$  Å, with frequencies comparable to those of the high-spin Cpd I. The Lowdin bond order of the Fe-O bond is 1.5 and 1.2 for the low- and high-spin states, respectively. Overall, within the single-reference ES the stretched Fe=O associated with the high-spin state is weaker and – being marginally higher than the low-spin state – is more likely to act as the hydrogen acceptor.

Table 2: Energies and FeO bond lengths for Cpd I/II computed at the B3LYP-D3/6-31G\* and B3LYP-D3/6-31+G\*\* levels. The energies are given with respect to the low-spin state of Cpd I;  $\Delta = E_{\text{CH}_4} - E_{\text{CH}_3}$  due to hydrogen abstraction is subtracted from the Cpd II energies.

method		6-31G* (full)		D3/6-31G* (CH <sub>3</sub> )			D3/6-31+G** (CH <sub>3</sub> )		
system	spin	Fe-O [Å]	E [kJ/mol]	Fe-O [Å]	E [kJ/mol]	$\tilde{\nu}$ [1/cm]	FeO [Å]	E [kJ/mol]	$\tilde{\nu}$ [1/cm]
Cpd I	low	1.656	0	1.651	0	714.5	1.654	0	685.9
Cpd I	high	1.698	2.44	1.713	2.64	538.8	1.714	3.44	542.0
Cpd II	low	1.818	72.7	1.808	63.95	531.2	1.820	41.40	528.9
Cpd II	high	1.823	45.9	1.822	37.25	514.5	1.835	16.12	510.8

Given the analysis of Cpd I and Cpd II above and of the apoenzyme,<sup>10</sup> all DFT calculations relevant to PES construction were performed at the unrestricted B3LYP-D3/6-31+G\*\* level of theory in gas phase using the post-reaction experimental crystal (solid state) structure for the ferric enzyme and heptanoic acid as the truncated substrate, as shown in Fig. 3. According to the experimental geometry, the fatty acid is deprotonated (the CO bonds of the carboxylic group are of equal length), implying that it should carry a negative charge. Since the enzyme carries a positive charge, this results in an overall charge-neutral model. After thorough testing of the spin-densities, however, we settle on a model with an overall charge of +1 and a neutral (protonated) fatty acid with the COO atoms space-fixed at the experimental geometry, because the electron density for this model shows the expected localization across Fe-S-ligand (as in Fig. SI1) compared to the DFT results for the charge-separated

system. Moreover, in the full OleT system the negative charge on the carboxyl group would be balanced by a positively charged arginine residue, as seen in Fig. 1.

Optimization of the positions of the acceptor oxygen and all hydrogen atoms (at the experimental geometry of the remaining heavy atoms) yields a donor-acceptor (DA) distance of 3.40/3.36 Å for the low/high spin-states, respectively. The Fe=O distances are within 0.01 Å of the values listed in Table 2 for Cpd I. These DA distances are too large for room-temperature HAT. However, it has been noted, that the substrate is rather flexible in our experimental temperature range. For example, in Ref.<sup>28</sup> it is argued that the process occurs at DA=2.7 Å, while the equilibrium DA value is 3.1 Å; fluorescence studies have revealed a significant degree of fatty acid mobility during the single turnover reaction,<sup>29</sup> and molecular dynamics simulations performed in Ref.<sup>30</sup> yield root-mean-squared deviation (RMSD) values of 1.10 Å for 8, 14, and 20-carbon substrates at 300 K.

With that in mind, we perform constrained geometry optimizations on a system in which the oxo- group is movable and the fatty acid is ‘pinned’ at the ends, i.e. the terminal carbon and carboxyl -COO are frozen, while the remaining atoms are allowed to relax. From this reactant state, the energy minimization yields even longer DA distances of 3.75/3.80 Å for the triplet/quintet states; these values, similar to those obtained by Du et. al.<sup>30</sup> for Cpd I interacting with various substrate lengths, are far too large for HAT. Inclusion of a movable water molecule into the model shortens the DA distance by  $\sim 0.2$  Å, yet this is still longer than that of the solid state structure. Therefore, to identify the HAT-*prepositioned* configuration we repeat the constrained optimization procedure beginning in the product (hydroxo-) state, where the transferring H has already been removed from the donor carbon on the acid. This process yields DA distances of 3.135 and 3.129 Å, and Fe-OH bond distances of 1.887 and 1.907 Å for the low- and high-spin states, respectively. Note that inclusion of the fatty acid stretches the Fe-O distance relative to the isolated Cpd II values (1.82 and 1.84 Å for the low- and high-spin states in Table 2). The mobility of the substrate atoms is comparable to that obtained from dynamics simulations on a larger Cpd II complex<sup>31</sup>

(excepting those that we artificially ‘pin’).

Reaction path configurations are obtained by scanning between the product-optimized geometries described above and a corresponding prepositioned-reactant state  $G_0$ , which is created by ‘reattaching’ the transferring hydrogen to the donor carbon and optimizing its position along with the position of the other bound hydrogen, keeping the rest of the system frozen. For clarity, the following labels are used, corresponding to Fig. 3: **A** = Acceptor oxygen, **D** = Donor carbon, **T** = Transferring hydrogen, and **B** = Bonded hydrogen. Using this notation and beginning from the  $G_0$  state, the energy profile is computed with a constrained **TA** distance (**A** is space-fixed) while **B** is relaxed – this captures the  $sp^3-sp^2$  switch of the donor orbitals during the transfer. The resulting high-spin reactant state is lower in energy than the low-spin state by 18 kJ/mol (4.3 kcal/mol) and exhibits a barrier of 81 kJ/mol (19.4 kcal/mol) at the TD distance of 1.58 Å (TA = 1.52 Å). The low-spin scan yields a maximum energy of 60 kJ/mol (14.3 kcal/mol) along the reaction path with respect to the reactant geometry. Both high- and low-spin energy profiles show discontinuities. Therefore, to analyze HAT we proceed the multi-reference ES calculations of a ‘hybrid’ reaction path. This path is defined by the lowest energy geometries from the two scans (whose optimized geometries are very similar) for a total of 14 points  $\{G_i\}$ ; selected geometries of this path are shown in Fig. 3. The reaction path coordinate  $x$  describing the correlated motion of **T** and **B**, is defined as the collective displacement of the two active hydrogens,

$$x_j = \sum_{i=1,j} \|G_i - G_{i-1}\|, \quad (1)$$

$$\|G_i - G_{i-1}\| = \left( \sum_{k=1,6} (r_{i,k} - r_{i-1,k})^2 \right)^{1/2}, \quad (2)$$

where  $k$  enumerates the coordinates of **T**,  $(r_1, r_2, r_3)$ , and of **B**,  $(r_4, r_5, r_6)$ . The effective mass is the same as that of hydrogen or deuterium, since the motion along the reaction path involves displacement of two physical particles of equal mass. Furthermore, we have explored

the effect of the acceptor oxygen’s motion during HAT by adding a second dimension,  $y$ , which describes the displacement of **A** from the HAT-prepositioned location ( $y = 0$  corresponds to Fe-O=1.907 Å). The hydrogen coordinate  $x$  is rescaled according to the  $y$ -values to generate the cartesian-space positions of **T**, **B**, and **A**.

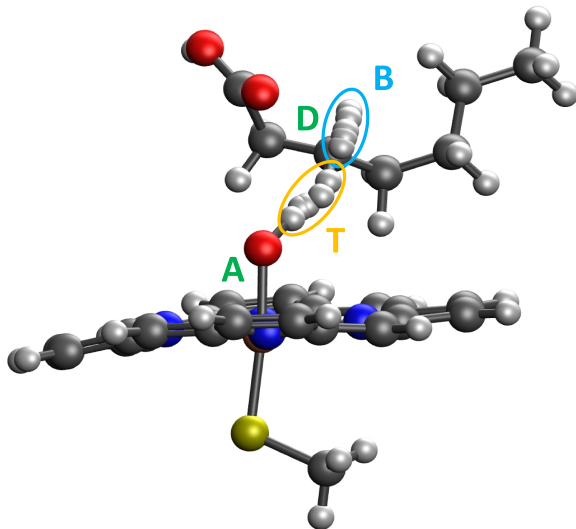


Figure 3: Geometry used to define the reaction path. **D** = donor carbon, **A** = acceptor oxygen, **T** = transferring hydrogen, **B** = hydrogen bonded to **D**. The path is defined by the energy minimization of **T** and **B** for a set of **TA** distances. Positions of the remaining atoms are described in text.

To summarize, the two dimensions of the reaction path PES,  $V(x, y)$ , are defined as follows. The first coordinate,  $x$  is the collective coordinate of the reactive hydrogen **T** and the other hydrogen **B** attached to the same carbon atom, i.e. to the donor **D**, as computed by the minimal energy path at the B3LYP-D3/6-31+G\*\* level of theory; the corresponding effective mass is that of a proton (or deuteron). The second coordinate,  $y$ , describes displacement of the oxygen atom along the Fe-O bond direction, as computed at the HAT-prepositioned geometry (referred to as  $G_0$  above) at the B3LYP-D3/6-31+G\*\* level; the corresponding mass is that of an oxygen nucleus. The multireference  $V(x, y)$  is computed with the Complete Active Space<sup>32</sup> CAS(4,6) method followed by the perturbative correction using Multi-Configuration Quasi-Degenerate Perturbation Theory (MCQDPT),<sup>33</sup> as implemented in GAMESS (v. June 30, 2019).<sup>26</sup> The active space is chosen based on the

orbital energy gaps computed at the reactant configuration; the orbital optimization and the subsequent perturbative corrections are performed on the lowest two nearly-degenerate energetic states, used with equal weights. Because of the high numerical cost of this ES method, we resort to modestly-sized basis sets: the m6-31G\* basis set<sup>34</sup> was used for all atoms except for the two optimized hydrogens **T** and **B**, which were represented by the 6-31G\*\* basis. The m6-31G\* basis is a ‘modified’ 6-31G\* basis which improves representation of the transition metals (in our case Fe); m6-31G\* is identical to 6-31G\* for all other atoms. The electronic structure model described above is used to compute 129 energy points, with about 17 points mapping the collective hydrogen coordinate  $x$  and a variable number of points along the Fe-O dimension  $y$ . These energies are then used in a least-squares fit of this surface by plane waves with frequencies ranging from  $\pi/(2L)$  to  $4\pi/(2L)$ , with  $L$  being the box size for each dimension. The data and the fit are provided in Supporting Information.

Unlike the DFT energy profiles, the resulting PES is smooth and, for the 1D slice based off of the  $G_0$  geometry ( $y = 0$ ), yields a barrier of 29 kJ/mol (6.9 kcal/mol), which is reasonably close to the experimental activation energy of 16 and 38 kJ/mol for the protonic and deuteronic HAT, respectively. (In general, the activation energy is not equal to the energy barrier.<sup>35</sup>) The global barrier on the 2D PES which involves the acceptor motion is significantly higher, however, because the strength of the Fe=O bond in the reactant configuration is overestimated. The three global extrema (and their locations in coordinate space) are the reactant well ( $x=-0.036 a_0, y=-0.87 a_0$ ), the barrier top ( $x=1.79 a_0, y=-0.43 a_0$ ), and the product well ( $x=3.32 a_0, y=0.01 a_0$ ). The global barrier height is 286.9 kJ/mol (68.57 kcal/mol), and the product well is 47.4 kJ/mol (11.3 kcal/mol) lower than the reactant well. We believe that the chosen ES model provides a qualitatively correct 2D PES for the HAT, although quantitatively it is limited by the small size of the basis, which is especially pronounced in the transition state region. As an attempt to correct for this, we calibrate our PES by examining a somewhat similar hydrogen transfer reaction,  $\text{OH} + \text{CH}_4 \rightarrow \text{OH}_2 + \text{CH}_3$ . By applying the same approach and multireference method, we obtain a reaction barrier of

52.2 kcal/mol for this reaction. A comparison of this number with the 6.7 kcal/mol value from the HTBH38 database<sup>36</sup> yields a corrective scaling factor of 7.8, applied to our original 2D PES for the HAT in OleT.

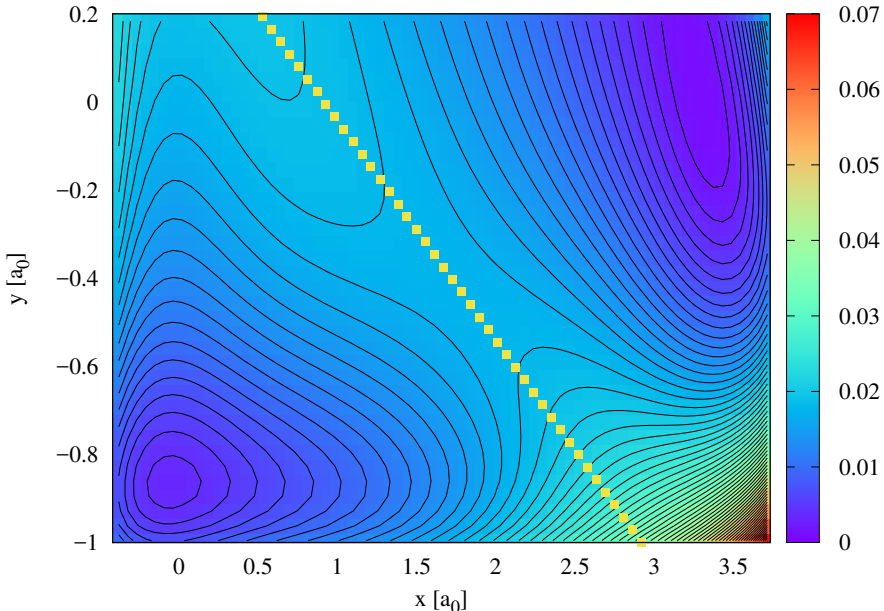


Figure 4: The contour plot of the scaled 2D PES (contours are spaced at 0.001 Hartree). The squares mark the separation for the reactant/product regions used in the analysis of the nuclear dynamics. The proton/transfer coordinate,  $x$ , and the oxygen displacement coordinate are given in bohr. The HAT-prepositioned geometry  $G_0$  corresponds to  $y = 0$ .

## 3.2 Proton/deuteron dynamics

### 3.2.1 KIE estimates from 2D wavepacket dynamics

Within the 2D model, the HAT reactants can be represented by a Gaussian wavepacket  $\psi_0$ ,

$$\psi_0 = \left( \frac{4\alpha_x\alpha_y}{\pi^2} \right)^{1/4} e^{-\alpha_x(x-x_0)^2 - \alpha_y(y-y_0)^2 + ip_x(x-x_0) + ip_y(y-y_0)}, \quad (3)$$

whose initial parameters are listed in Table 3. The Gaussian width parameters  $\alpha_x$  and  $\alpha_y$  are determined by the ground-state harmonic vibrational frequencies. The wavepacket is centered at the bottom of the reactant well, with the momentum components  $p_x$  and  $p_y$  chosen

to be positive (to mimic bond stretching) and commensurate to the thermal energy of the systems. The dynamics is performed for a set of temperatures,  $T = \{250, 275, 300, 325, 350\}$  K.

Table 3: The grid and wavepacket parameters, listed in the appropriate atomic units, for the 2D reaction path dynamics on scaled PES. <sup>a</sup> The initial wavefunction  $\psi_0$  of Eq. (3) used in the SOFT dynamics with initially stretched Fe-O bond is modified by assigning  $y_0 = -0.65$   $a_0$ .

Hamiltonian diagonalization				
grid size	$x_{min}$	$x_{max}$	$y_{min}$	$y_{max}$
$96 \times 96$	-1.1	4.3	-1.4	1.8
SOFT propagation				
grid size	$x_{min}$	$x_{max}$	$y_{min}$	$y_{max}$
$256 \times 256$	-1.7	4.3	-1.4	1.8
Initial wavefunction <sup>a</sup>				
$\alpha_x^H$	$\alpha_x^D$	$\alpha_y^O$	$x_0$	$y_0$
4.21	5.95	46.43	-0.0365	-0.868

First, we examine wavepacket probabilities computed with the Miller-Colbert Discrete Variable Representation of the Hamiltonian,<sup>37</sup> equivalent to representing a wavefunction on an equidistant 2D grid. The parameters defining the grid are listed in Table 3; the grid size is limited to a matrix size of  $10^4 \times 10^4$  elements by the standard LAPACK libraries<sup>38</sup> employed to diagonalize the Hamiltonian matrix. We calculate both the survival and reaction probabilities defined in the following manner: the survival probability, i.e. occupation of the reactant well,  $P^r$  is computed as

$$P^r(t) = \int \int_{x < x_c} |\psi(x, y, t)|^2 dx dy, \quad x_c = 1.5 \text{ a}_0 \quad (4)$$

while the reaction probability  $P^p$  is computed on the product subspace defined by  $y_c = -0.5x - 0.468$  (shown in Fig. 4),

$$P^p(t) = \int \int_{y > y_c} |\psi(x, y, t)|^2 dx dy. \quad (5)$$

The wavepacket dynamics is characterized by quasi-oscillations of the survival probability  $P^r$

(Fig. 5(a)), which are unphysical and come from the lack of bath modes needed to dissipate the energy of the moving atoms upon completion of HAT. The reaction probability  $P^p$  also changes at long times, though the oscillatory pattern is less visible there. We thus estimate the wavepacket reaction probabilities from the first plateau region of  $P^p$  (Fig. 5(b)) for  $t < 2500$  a.u. and  $t < 4000$  a.u. for the hydrogen and deuterium particles, respectively. The ratio of these two probabilities, used as a measure of the KIE and listed in Table 4, is on the order of  $\sim 3.5$  and is essentially temperature independent. This computed temperature dependence is underestimated compared to the experimental KIE, the latter of which is reduced by a factor of  $\sim 2$  over the temperature range of [277, 294] K. A possible reason for this discrepancy is that the reactive wavepacket dynamics is physically meaningful only over short times (one quasi-oscillation period) in the bound double-well potential model, where it is also dominated by over-the-barrier probability flow. Access to the tunneling regime requires longer propagation times and modifications to either the potential or to the model to prevent the back-reaction. To this end, we have also examined the reaction probabilities obtained from wavepacket time-propagation in the presence of an absorbing potential in the product well region. The initial wavefunction of Eq. (3) is evolved in time for up to  $t_f = 6000$  a.u. on a grid of  $256 \times 256$  equidistant points using the split-operator/Fourier transform (SOFT) approach.<sup>39,40</sup> SOFT does not involve matrix construction and diagonalization, thus allowing larger spatial grids. A linear imaginary absorbing potential

$$V_I = 0.5(x - x_i), \text{ for } x > x_i, \quad (6)$$

has been added to mitigate the reflection of the wavefunction back towards the reactant domain. The wavepacket and time-propagation parameters are given in Table 3. The overall transmission probability  $P$  is defined as the time-integral over the finite propagation time  $t_f$

of the probability flux function  $j$  across a dividing surface<sup>41</sup> located at  $x_i$  nearest to  $2 a_0$ .

$$j(t) = \frac{1}{2m_H} \int_{y_{min}}^{y_{max}} dy \left( \psi_t^* \frac{\partial \psi_t}{\partial x} - \psi_t \frac{\partial \psi_t^*}{\partial x} \right) \Big|_{x=x_c}, \quad (7)$$

$$P(t_f) = \int_0^{t_f} j(t) dt. \quad (8)$$

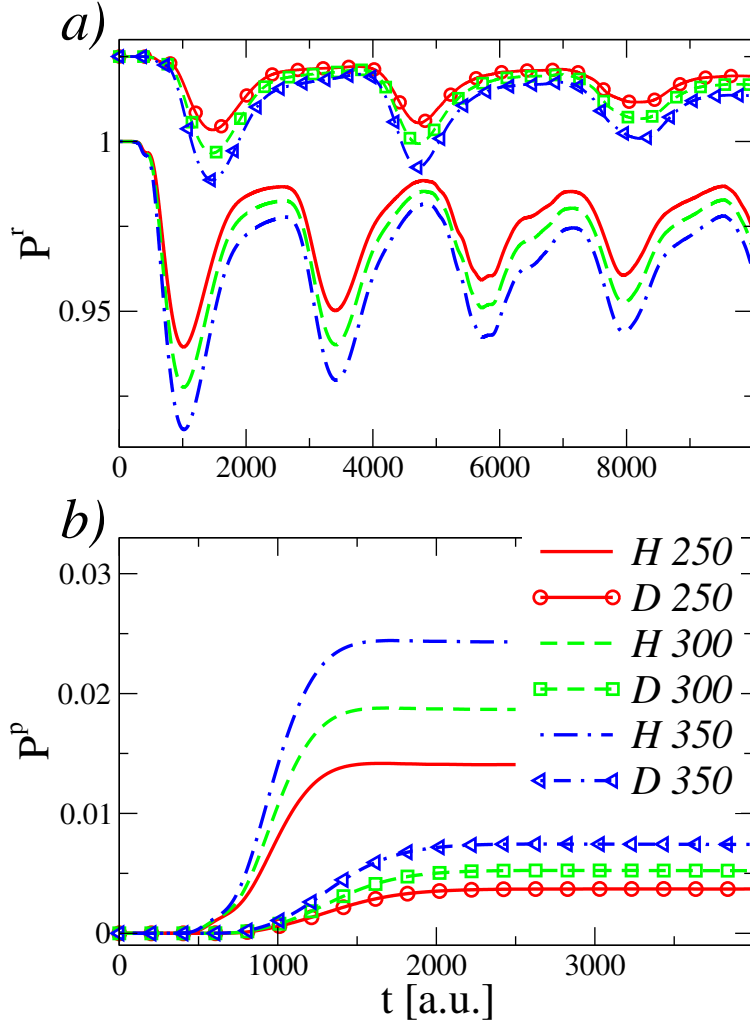


Figure 5: The wavepacket dynamics representing HAT in OleT for the scaled 2D reaction path model. (a) The survival probability  $P^r$ , and (b) the reaction probability  $P^p$  of Eqs. 4 and 5 as functions of time  $t$ . The deuterium curves in panel (a) are shifted vertically by 0.025 for clarity. In panel (b)  $P^p$  is shown only for the times used to estimate the KIE. The temperatures (K) and isotopes indicated on the legend are applicable to both panels.

Since, as argued above, the HAT proceeds for DA separations shorter than the 0K equi-

librium values,  $\psi_0$  has been initialized both in the reactant well minimum and at the oxygen position displaced by  $0.22 a_0$ , representing a stretched Fe-O bond. The H transmission probabilities and KIE values are listed in Table 4. The corresponding flux functions are displayed in Fig. 6; the most prominent peak occurs at  $t \approx 850$  a.u. for H and  $t \approx 1350$  a.u. for D, regardless of temperature and starting configuration. Smaller peaks can be seen at regular intervals with increasing  $t$ ; this time-dependence corresponds to small-amplitude motion of the wavepacket in the reactant well. The reaction probabilities in the SOFT simulations are somewhat larger than those obtained from the shorter-time (single oscillation) evolution of the wavepackets reconstructed from the eigenvectors/eigenvalues of the real Hamiltonian; however, the KIE and its temperature dependence obtained for the reactant-well-centered  $\psi_0$  are quite similar to those of the diagonalization approach. This means that the tunneling regime associated with larger KIE values is still not fully captured. The dynamics initiated with the stretched Fe-O geometry yields larger HAT probabilities and smaller KIE values, which is expected given the energetic nature of this configuration. Therefore, to reproduce the experimental KIE and its temperature-dependence, we switch to a model that isolates the tunneling mechanism, and compute the tunneling contribution to thermal reaction rate constants using the energy-resolved probabilities along 1D  $x$ -scans of the original (unscaled) 2D PES, characterized by a barrier close to the experimental activation energy for  $y = 0$ .

Table 4: The wavepacket reaction probabilities and KIE values for the protonic HAT obtained from Hamiltonian diagonalization (columns 2 and 3), SOFT propagation of  $\psi_0$  centered in the reactant well (columns 4-5), and SOFT propagation initialized in the stretched Fe-O configuration (columns 6-7). See text for details.

T [K]	$P^p$	$\text{KIE}^{diag}$	$P^{SOFT}$	$\text{KIE}^{SOFT}$	$P_{str}^{SOFT}$	$\text{KIE}_{str}^{SOFT}$
250	0.0142	3.83	0.0192	3.611	0.0489	2.688
275	0.0164	3.72	0.0214	3.524	0.0546	2.590
300	0.0188	3.595	0.0239	3.410	0.0606	2.496
325	0.0215	3.43	0.0265	3.280	0.0668	2.407
350	0.0244	3.28	0.0294	3.144	0.0733	2.323

To justify this switch to a 1D model, let us consider the current 2D PES with the following question in mind: does it make sense to describe HAT as an adiabatic process

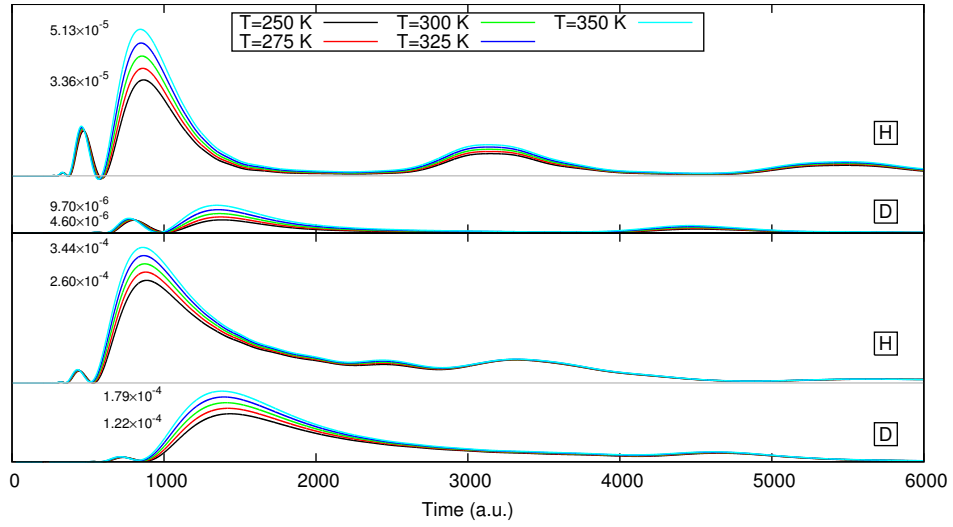


Figure 6: Flux functions  $j(t)$  for configurations 1 (top) and 3 (bottom). A vertical shift has been applied to distinguish the H and D curves from one another in each case; their relative amplitudes are consistent within a given panel, but scaled across the panels for visual clarity. A faint grey line indicates the zero position for the H isotope curves. The maxima for the 250 and 350 K curves are labeled for each configuration.

under the rationale of timescale separation? In other words, is it reasonable to ‘freeze’ the acceptor position and analyze the isolated dynamics along the CH stretch? Certain insight can be gained from the Hamiltonian eigenvectors relevant to tunneling. Heat maps of the lowest energy tunneling *pairs* of states, defined as having reactant/product region occupations  $P$  of at least 0.1, are shown in Fig. 7. Panels (a) and (b) show the protium states  $n = \{44, 45\}$ , with energies that are  $\sim 95.57\%$  of the barrier height and split by 1.3 kJ/mol (0.31 kcal/mol). Their structure is characterized by a high excitation along the oxygen-displacement coordinate  $y$ . The deuterium counterparts (panels (c,d)) are characterized by a higher excitation in the collective hydrogen coordinate  $x$ : the energies of these states,  $n = \{59, 60\}$ , are  $\sim 94.35\%$  of the barrier height and their splitting is 2.3 kJ/mol (0.55 kcal/mol). The nodal pattern in the probability density for these states is characteristic of the ‘direct product’ function, which is factorizable in  $x$  and  $y$ . This suggests that below-the-barrier HAT is largely decoupled from the acceptor oxygen motion along  $y$ , and the hydrogen is transferred along  $x$  once the Fe-O bond is stretched, possibly as a result of thermal motions of the molecular environment. In case of deuterium, both the Fe-O and C-D stretches are excited, and the probability density pattern has more  $xy$  correlation, though the nodes due to excitations in  $x$  and  $y$  are easily discernible. This is consistent with D being twice heavier than H and more strongly coupled to the oxygen atom.

Overall, we conclude that the adiabatic treatment of HAT in the tunneling regime is reasonable, and we thus proceed with 1D slices of the original 2D PES describing stretched Fe-O geometries for which the barriers to HAT are in the range of the activation energies obtained from experimental reaction rates. In particular, the barrier along the hydrogen-donor distance coordinate for the stretched Fe-O configuration of 1.9 Å (corresponding to the optimized produce state geometry) reduces to approximately 30 kJ/mol and yields KIE trends consistent with the kinetics data.

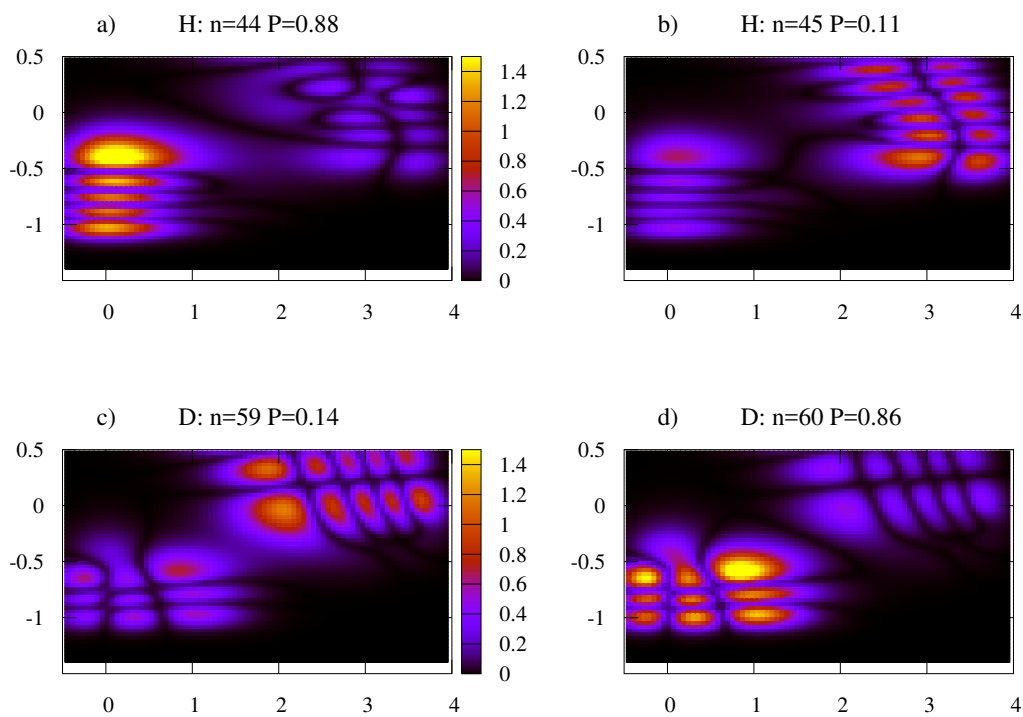


Figure 7: Selected eigenfunctions on the 2D PES. The tunneling reactant/product pairs are shown in panels (a-b) are (c-d) for the protium and deuterium isotopes, respectively. The eigenfunction label  $n$  and the reactant region occupation  $P$  are printed above each panel.

### 3.2.2 KIE based on the 1D reaction rate constants

In this section we model proton/deuteron transmission across the 1D reaction path, examining the isotope effects on the activation energy and the KIE, which is defined as the ratio of the reaction rate constants. The KIE is then constructed as the product of the zero point energy (ZPE) contribution,  $KIE^{ZPE}$ , due to the vibrational partition function and the barrier transmission (including tunneling) contribution,  $KIE^t$ , due to the difference in transmission probabilities across the barrier,

$$KIE = \frac{k_H}{k_D} \approx KIE^t \times KIE^{ZPE}. \quad (9)$$

Formally, an additional binding isotope effect (BIE) term can be included into an ‘apparent’ KIE to account for preferential *binding* of the protiated/deuterated substrate to the enzyme;<sup>42</sup> however, this is omitted in the current analysis as we anticipate it will have negligible impact on our system. More specifically, since the process of substrate binding is already a prerequisite for Cpd I formation<sup>3</sup> (which is itself the starting point for our model), we conclude that the role of the BIE is not a concern for the present study. Given the typical frequency of the CH(D) stretch of 2800(2000) 1/cm, only the ground vibrational state is populated at room temperature, meaning the dominant contribution to the KIE comes from differences in the vibrational ZPE of the isotopologues. Within the one-dimensional model of the reaction path, in which the ZPE correction at the transition state is neglected, this effect,

$$KIE^{ZPE} = \exp\left(\frac{\omega_H - \omega_D}{2k_B T}\right), \quad (10)$$

is  $\sim 6 - 7$  at  $T = 300\text{K}$  depending on the position of the oxygen atom. Typically, the tunneling correction is made within the parabolic approximation to the PES (e.g. the Wigner correction), which accounts for shallow tunneling at thermal energies comparable to the barrier,<sup>43</sup> or using quasiclassical approaches, such as the Wentzel-Kramers-Brillouin (WKB) approximation to account for deep tunneling.<sup>44</sup> Here we perform exact quantum dynam-

ics covering all tunneling regimes along the one-dimensional reaction path coordinate  $x$  for fixed positions of the acceptor  $y$ . The thermal reaction rate constants,  $k(T)$ , are obtained from the energy-resolved transmission probabilities obtained within the wavepacket correlation approach of Tannor and Weeks.<sup>45</sup> The 1D scattering potentials are constructed by setting the potential beyond the well-minima to an appropriate constant as shown in Fig. 8. The key parameters of the PES curves are listed in Table 5. Further details are given as Supplementary Information.

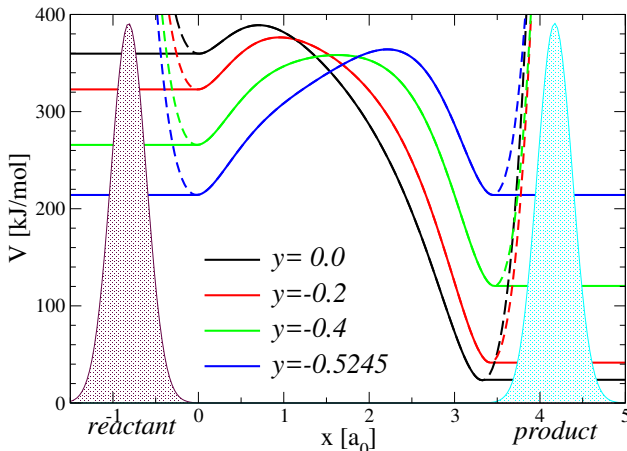


Figure 8: The potential energy profiles for selected positions of the acceptor oxygen  $y$ :  $y = 0$  corresponds to the HAT-prepositioned geometry,  $y = 0.5245 a_0$  corresponds to the reactant and product barrier of equal depth. The Gaussians to the left and to the right of the barriers represent the initial reactant and product wavepackets.

Table 5: The parameters of the reactant well and barrier for the one-dimensional PES profiles. The frequencies for the deuterium are smaller than those for the protium by a factor of  $\sqrt{m_H/m_D} \approx 1.41$ .

$y [a_0]$	$x^r [a_0]$	$w^r [\text{cm}^{-1}]$	$x^b [a_0]$	$w^b [\text{cm}^{-1}]$	$V^b [\text{kJ/mol}]$
0.0	0.009	2500.0	0.707	1369.1	29.3
-0.2	-0.005	2748.6	0.951	1170.1	53.6
-0.4	-0.015	2874.4	1.629	783.8	92.5
-0.5245	-0.019	2895.9	2.214	1291.8	149.9

The resulting KIE is shown in Fig. 9(a); inclusion of the ZPE energy effect (not shown) increases the KIE values by a factor of 6–7. Both the barrier height and its shape influence the KIE: the most classical-like value ( $\text{KIE}^t \sim 1.3$ ) is obtained for  $y = 0.4 a_0$ , which is not

the highest but the widest barrier out of the four PES slices. The nuclear quantum effect on the barrier transmission, summarized in Table 6, is quantified by comparing the quantum and classical thermally averaged transmission probabilities. Denoting the barrier height as  $V^b$  and treating the particle as classical, i.e.  $N(E) = 1$  for  $E > V_b$  and zero otherwise, the classical rate constant is

$$k^{cl}(T) = \frac{k_B T}{Q} e^{-\beta V^b}. \quad (11)$$

The ratio of the quantum and classical rate constants define the tunneling factor  $\kappa$

$$\kappa(T) = \frac{k^{qm}(T)}{k^{cl}(T)}, \quad (12)$$

which is used as a measure of the quantum contribution. The Boltzmann-averaged probabilities  $kQ$  and the tunneling factors are listed in Table 6. The KIE values are given for the partition function of the translational motion. These results show that the measured KIE and its temperature dependence are consistent with the acceptor displacement of  $y = [-0.2, 0]$ . At  $y = -0.4 \text{ a}_0$  the HAT is too ‘classical’ – the KIE is essentially is temperature-independent; at  $y = -0.5245 \text{ a}_0$  its temperature dependence is too strong ( $\eta \sim 3.1 - 3.5$ ).

Table 6: HAT modeled along one-dimensional paths defined by  $y$ . The reaction rate constants, given as  $kQ$ , the tunneling factors,  $\kappa$ , and KIEs are listed at  $T = 300 \text{ K}$ . The ratio of the rate constants over the experimental temperature span,  $\eta = \text{KIE}_{294.55} / \text{KIE}_{277.25}$ , is listed in parentheses in the KIE columns. The classical KIE due to the barrier transmission is equal to  $\sqrt{m_H/m_D} \approx 1.41$  for all temperatures and all values of  $y$ .

$y \text{ [a}_0]$	$k^{cl}Q$	$k_H^{qm}Q$	$\kappa_H$	$k_D^{qm}Q$	$\kappa_D$	KIE <sup>t</sup> ( $\eta$ )	KIE ( $\eta$ )
0.0	7.52e-09	9.75e-08	13.0	2.41e-08	3.2	5.7 (1.3)	34.7 (1.4)
-0.2	4.42e-13	4.09e-12	9.2	9.71e-13	2.2	6.0 (1.6)	40.0 (1.8)
-0.4	7.45e-20	1.39e-19	1.9	9.95e-20	1.3	2.0 (1.1)	13.8 (1.2)
-0.5245	7.55e-30	2.04e-28	26.9	2.09e-29	2.8	13.8 (3.1)	96.1 (3.5)
experiment	$T = 294.55 \text{ K}$		KIE= $15.2 \pm 1.2$			$\eta = 1.8$	

The activation energy, defined as,<sup>35</sup>

$$E_A(\beta) = -\frac{d \ln k(\beta)}{d\beta}, \quad (13)$$

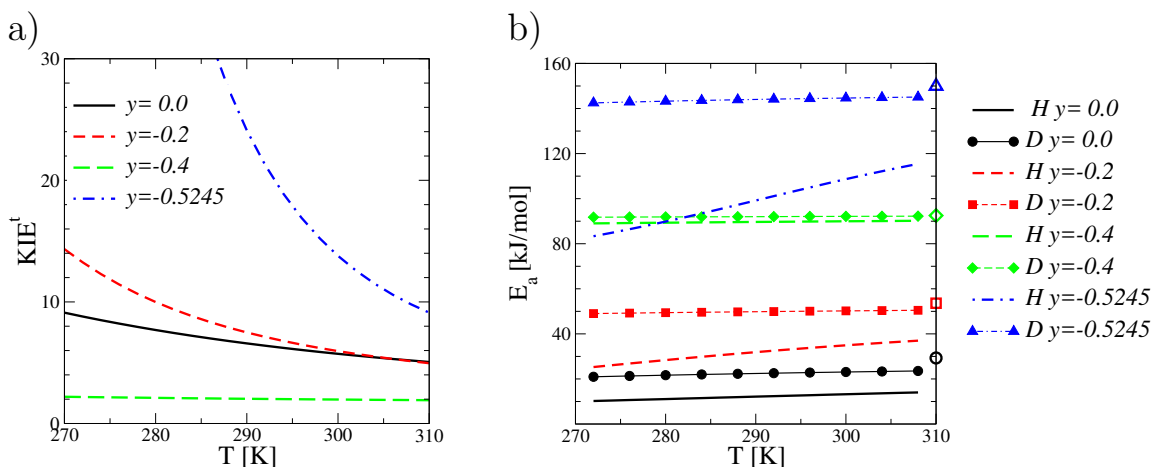


Figure 9: OleT: the temperature dependence (a) of the transmission  $\text{KIE}^t$ , and (b) of the activation energy  $E_a$  computed from Eq. (13) for the hydrogen and deuterium systems. In panel (b) filled symbols mark  $E_a$  for the deuterium; the open symbols on the right-hand-side indicate the respective analytic barrier heights. The acceptor displacement  $y$  in the legend is given in  $a_0$ .

is shown for hydrogen and deuterium transfer in Fig. 9(b). For the heavier isotope,  $E_a$  shows weak temperature dependence and is closer to the classical barrier top (marked with open symbols) of the corresponding  $y$  value. For the lighter isotope, the dependence of  $E_a$  on the temperature is more appreciable. At the middle of the experimental temperature range,  $T = 285$  K, the computed  $E_a$  for H(D) is  $\sim 11(22)$  kJ/mol ( $2.6(5.3)$  kcal/mol) at  $y = 0.0$  and  $30(50)$  kJ/mol ( $7.2(12)$  kcal/mol) at  $y = -0.2 a_0$ , which are the closest values to the experimental estimates for  $E_a$  of  $16.7(38.7)$  kJ/mol ( $3.99(9.25)$  kcal/mol). From the KIE *change* over the experimental temperature range (Fig. 10), the results for the acceptor displacement of  $y = [-0.2, 0.0] a_0$  give the best agreement between the computed (ZPE included) and experimentally observed temperature-dependence of the KIE. The transmission-only KIE computed for  $y = -0.2 a_0$  gives the best overall agreement with experimental data.

## 4 Summary

We have presented an experimental/theoretical investigation of the hydrogen atom transfer (HAT) by the high-valent ferryl cytochrome P450(CYP) intermediate (Cpd I). For the first

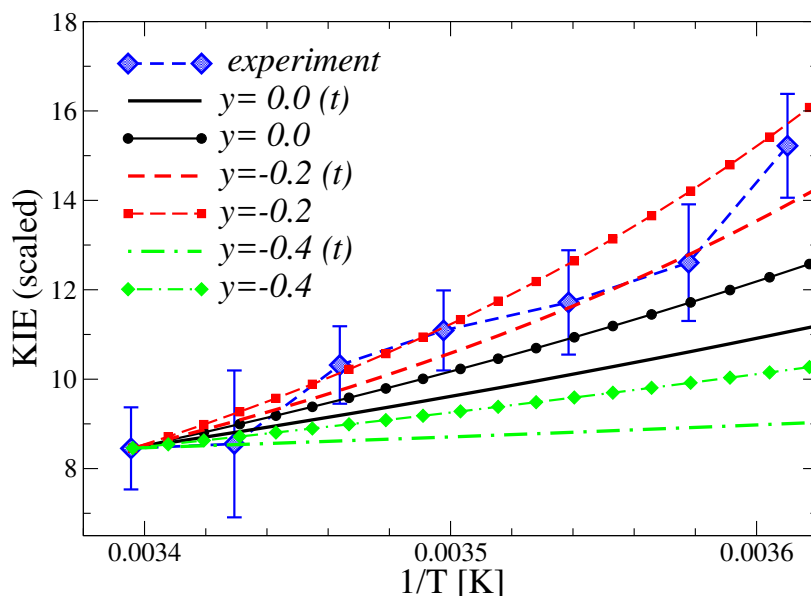


Figure 10: The KIE change over the experimental temperature range: the computed KIE is divided by the experimental value at the highest temperature. The curves with/without the symbols indicate the full and transmission KIEs. The acceptor displacement  $y$  in the legend is in  $a_0$ .

time the temperature-dependent rate constants and the substrate  $^2\text{H}$  kinetic isotope effect have been measured for CYP, yielding the KIE of 10-15 near 300K. The thermodynamics data for C-H bond activation barriers and the temperature dependence of the  $^2\text{H}$  KIE provide unique access to the parameters of a ferryl intermediate in aCYP, and more globally, any mononuclear  $\text{Fe}^{4+}$ -oxo system to date. To gain insight into this HAT, based on the experimental crystal structure of the enzyme, we have developed a molecular model, composed of the central Fe atom ligated by a hydrated porphyrin ring and an axial  $-\text{SCH}_3$  group and the fatty acid represented by a ‘pinned’ heptanoic acid molecule. The DFT-based electronic structure analysis established a precursor reaction path for HAT from the fatty acid to the oxo-enzyme. These calculations were then refined using the CAS(4,6)-MCQDPT multireference method, resulting in a 2D PES consisting of C-H (with hybridization of the remaining H) and Fe-O stretch coordinates. This PES was then empirically scaled by a factor of 7.8, based on benchmark calculations of the  $\text{OH} + \text{CH}_4 \rightarrow \text{CH}_3 + \text{H}_2\text{O}$  reaction which brought the energy barrier height close to the activation energies obtained from experiments.

Subsequently, KIE values across the temperature range [250-350] K were computed for a Gaussian wavepacket representation of the reduced 2D system at both short ( $t \in [2500-4000]$  a.u.) and intermediate ( $t=6000$  a.u.) time dynamics using the Miller-Colbert DVR basis representation of the Hamiltonian and the split-operator/Fourier transform (SOFT) approach, respectively. Both dynamics yield a similar temperature dependence for both the wavepacket reaction probabilities  $P^p$  and the overall KIE; however, the computed KIE was  $\sim 4$  times lower than the experimental value and underestimated the temperature dependence. Thus, neither approach correctly captured the tunneling behavior necessary to reproduce the experimentally-observed KIE trends.

Upon examination of the tunneling eigenvectors for the H and D isotopes, it was rationalized that an adiabatic picture for HAT is appropriate, and scattering calculations on multiple 1D slices of the unscaled 2D PES (corresponding to fixed distances of the Fe-O stretch) were performed. The experimental activation energy was well-approximated by the 1D barriers for the largest Fe-O stretch distances (i.e. the product Fe-O bond length) of  $1.8 - 1.9 \text{ \AA}$ ; these PES slices also reasonably reproduced the KIE temperature dependence and the isotope-dependence of the activation energy.

Based on the experimental data and theoretical modeling, the HAT in this system proceeds in the moderate tunneling regime, after the donor-acceptor distance is reduced compared to the solid state value due to thermal fluctuations. This explains the observed KIE values of  $\sim 8 - 16$  over the experimental range of temperatures. We also argue that the HAT reaction path is of multireference character due to intersecting low- and high- spin states of the single-reference treatment. Future work will involve a comparison of HAT in the wild-type OleT and its mutant species, which will give insight into the role of the ligand as a way to control ferryl during cytochrome P450 fatty acid decarboxylation.

## Supporting Information Available

Details of the energy-resolved transmission probability calculation and data and code for the two-dimensional potential energy surface.

## Acknowledgement

This material is based upon work supported by the National Science Foundation under Grant No. CHE-1056188 and CHE-1565985 (SG) and Grant 1555066 (TMM). The research used an XSEDE<sup>46</sup> allocation TG-DMR110037 and the UofSC HPC cluster, funded by the National Science Foundation under Grant No. CHE-1048629.

## References

- (1) Krest, C.; Silakov, A.; Rittle, J.; Yosca, T.; Onderko, E.; Calixto, J.; Green, M. Significantly Shorter Fe-S Bond in Cytochrome P450-I Is Consistent with Greater Reactivity Relative to Chloroperoxidase. *Nature Chem.* **2015**,
- (2) Grant, J. L.; Hsieh, C. H.; Makris, T. M. Decarboxylation of Fatty Acids to Terminal Alkenes by Cytochrome P450 Compound I. *J. Am. Chem. Soc.* **2015**, *137*, 4940–4943.
- (3) Grant, J. L.; Mitchell, M. E.; Makris, T. M. Catalytic Strategy for Carbon-Carbon Bond Scission by the Cytochrome P450 OleT. *Proc. Natl. Acad. Sci. U.S.A.* **2016**, *113*, 10049–10054.
- (4) Ricciardi, G.; Baerends, E. J.; Rosa, A. Charge Effects on the Reactivity of Oxoiron(IV) Porphyrin Species: A DFT Analysis of Methane Hydroxylation by Polycationic Compound I and Compound II Mimics. *ACS Catalysis* **2016**, *6*, 568–579.
- (5) Daniel, R.; Dunn, R.; Finney, J.; Smith, J. The Role of Dynamics in Enzyme Activity. *Annu. Rev. Biophys. Biomol. Struct.* **2003**, *32*, 69–92.

- (6) Henzler-Wildman, K. A.; Lei, M.; Thai, V.; Kerns, S. J.; Karplus, M.; Kern, D. A Hierarchy of Timescales in Protein Dynamics is Linked to Enzyme Catalysis. *Nature* **2007**, *450*, 913–916.
- (7) Klinman, J. P.; Kohen, A. Hydrogen Tunneling Links Protein Dynamics to Enzyme Catalysis. *Annu. Rev. Biochem.* **2013**, *82*, 471–496.
- (8) Klinman, J. P.; Offenbacher, A. R.; Hu, S. Origins of Enzyme Catalysis: Experimental Findings for C–H Activation, New Models, and Their Relevance to Prevailing Theoretical Constructs. *J. Am. Chem. Soc.* **2017**, *139*, 18409–18427.
- (9) Klinker, E. J.; Shaik, S.; Hirao, H.; Que Jr., L. A Two-State Reactivity Model Explains Unusual Kinetic Isotope Effect Patterns in C-H Bond Cleavage by Nonheme Oxoiron(IV) Complexes. *Angew. Chem. Int. Ed.* **2009**, *48*, 1291–1295.
- (10) Dutra, M.; McElhenney, S.; Manley, O. M.; Rassolov, V.; Makris, T. M.; Garashchuk, S. The Ligand Effect on the Electronic Structure of CYP 450. *submitted* **2022**,
- (11) Faponle, A. S.; Quesne, M. G.; de Visser, S. P. Origin of the Regioselective Fatty-Acid Hydroxylation Versus Decarboxylation by a Cytochrome P450 Peroxygenase: What Drives the Reaction to Biofuel Production? *Chem. Eur. J.* **2016**, *22*, 5478–5483.
- (12) Bathelt, C. M.; Zurek, J.; Mulholland, A. J.; Harvey, J. N. Electronic Structure of Compound I in Human Isoforms of Cytochrome P450 from QM/MM Modeling. *J. Am. Chem. Soc.* **2005**, *127*, 12900–12908.
- (13) Pu, J.; Gao, J.; Truhlar, D. G. Multidimensional Tunneling, Recrossing, and the Transmission Coefficient for Enzymatic Reactions. *Chem. Rev.* **2006**, *106*, 3140–3169.
- (14) Jakowski, J.; Huang, J.; Garashchuk, S.; Luo, Y.; Hong, K.; Keum, J.; Sumpter, B. G. Deuteration As a Means to Tune Crystallinity of Conducting Polymers. *J. Phys. Chem. Lett* **2017**, *8*, 4333–4340.

- (15) Soudackov, A. V.; Hammes-Schiffer, S. Proton-Coupled Electron Transfer Reactions: Analytical Rate Constants and Case Study of Kinetic Isotope Effects in Lipoyxygenase. *Faraday Discuss.* **2016**, *195*, 171–189.
- (16) Jevtic, S.; Anders, J. A Qualitative Quantum Rate Model for Hydrogen Transfer in Soybean Lipoyxygenase. *J. Chem. Phys.* **2017**, *147*, 114108.
- (17) Howe, G. W.; van der Donk, W. A. Temperature-Independent Kinetic Isotope Effects As Evidence for a Marcus-like Model of Hydride Tunneling in Phosphite Dehydrogenase. *Biochemistry* **2019**, *58*, 4260–4268.
- (18) Amaya, J. M. Mechanisms of Decarboxylation in the CYP152 Family of Cytochrome P450S. Ph.D. thesis, University of South Carolina, 2018.
- (19) Mitra, K.; Green, M. T. Reduction Potentials of P450 Compounds I and II: Insight into the Thermodynamics of C–H Bond Activation. *J. Am. Chem. Soc.* **2019**, *141*, 5504–5510.
- (20) Kohen, A.; Klinman, J. P. Enzyme Catalysis: Beyond Classical Paradigms. *Acc. Chem. Res.* **1998**, *31*, 397–404.
- (21) Shaik, S.; Kumar, D.; de Visser, S. P.; Altun, A.; Thiel, W. Theoretical Perspective on the Structure and Mechanism of Cytochrome P450 Enzymes. *Chem. Rev.* **2005**, *105*, 2279–2328.
- (22) Shao, Y.; Gan, Z.; Epifanovsky, E.; Gilbert, A. T. B.; Wormit, M.; Kussmann, J.; Lange, A. W.; Behn, A.; Deng, J.; Feng, X.; et al., Advances in Molecular Quantum Chemistry Contained in the Q-Chem 4 Program Package. *Mol. Phys.* **2015**, *113*, 184–215.
- (23) IQmol 2.14. web, <http://iqmol.org/>.

- (24) Spartan'18. Wavefunction, Inc. Irvine, CA. <http://www.wavefun.com/products/spartan.html>.
- (25) Maple 18. Maplesoft, a division of Waterloo Maple Inc., Waterloo, Ontario.
- (26) Schmidt, M.; Baldrige, K. K.; Boatz, J. A.; Elbert, S. T.; Gordon, M. S.; Jensen, J. H.; Koseki, S.; Matsunaga, N.; Nguyen, K. A.; Su, S. J.; Windus, T. L.; Dupuis, M.; Montgomery, J. A. GAMESS. *J. Comp. Chem* **1993**, *14*, 1347–1363.
- (27) Wang, L.; Mazzuca, J. W.; Garashchuk, S.; Jakowski, J. The Hybrid Quantum Trajectory/Electronic Structure DFTB-based Approach to Molecular Dynamics. Proceedings of the 2014 Annual Conference on Extreme Science and Engineering Discovery Environment. 2014; pp 24:1–24:8.
- (28) Klinman, J. P.; Offenbacher, A. R.; Hu, S. Origins of Enzyme Catalysis: Experimental Findings for CH Activation, New Models, and Their Relevance to Prevailing Theoretical Constructs. *J. Am. Chem. Soc.* **2017**, *139*, 18409–18427.
- (29) Amaya, J. A.; Rutland, C. D.; Leschinsky, N.; Makris, T. M. A Distal Loop Controls Product Release and Chemo- and Regioselectivity in Cytochrome P450 Decarboxylases. *Biochemistry* **2018**, *57*, 344–353.
- (30) Du, J.; Liu, L.; Guo, L. Z.; Yao, X. J.; Yang, J. M. Molecular Basis of P450 OleT(JE): An Investigation of Substrate Binding Mechanism and Major Pathways. *J. Comput. Aided Mol. Des.* **2017**, *31*, 483–495.
- (31) Bharadwaj, V. S.; Kim, S.; Guarnieri, M. T.; Crowley, M. F. Different Behaviors of a Substrate in P450 Decarboxylase and Hydroxylase Reveal Reactivity-Enabling Actors. *Sci. Rep.* **2018**, *8*.
- (32) Ivanic, J.; Ruedenberg, K. Identification of deadwood in configuration spaces through general direct configuration interaction. *Theor. Chem. Acc.* **2001**, *106*, 339–351.

- (33) Nakano, H. Quasidegenerate Perturbation Theory with Multiconfigurational Self-Consistent-Field Reference Functions. *J. Chem. Phys.* **1993**, *99*, 7983–7992.
- (34) Mitin, A. V.; Baker, J.; Pulay, P. An Improved 6-31G\* Basis Set for First-Row Transition Metals. *J. Chem. Phys.* **2003**, *118*, 7775–7782.
- (35) Hand, M. R.; Rodriguez, C. F.; Williams, I. H.; Balint-Kurti, G. G. Theoretical Estimation of the Activation Energy for the Reaction  $\text{HO} + \text{H}_2\text{O} \rightarrow \text{H}_2\text{O} + \text{OH}$ : Importance of Tunneling. *J. Phys. Chem. A* **1998**, *102*, 5958–5966.
- (36) Zhao, Y.; Lynch, B. J.; Truhlar, D. G. Multi-Coefficient Extrapolated Density Functional Theory for Thermochemistry and Thermochemical Kinetics. *Phys. Chem. Chem. Phys.* **2005**, *7*, 43–52.
- (37) Colbert, D. T.; Miller, W. H. A Novel Discrete Variable Representation for Quantum Mechanical Reactive Scattering via the S-matrix Kohn Method. *J. Chem. Phys.* **1992**, *96*, 1982–1991.
- (38) Anderson, E.; Bai, Z.; Bischof, C.; Blackford, S.; Demmel, J.; Dongarra, J.; Du Croz, J.; Greenbaum, A.; Hammarling, S.; McKenney, A.; Sorensen, D. *LAPACK Users' Guide*, 3rd ed.; Society for Industrial and Applied Mathematics: Philadelphia, PA, 1999.
- (39) Kosloff, R. Time-Dependent Quantum-Mechanical Methods for Molecular Dynamics. *J. Phys. Chem.* **1988**, *92*, 2087–2100.
- (40) Feit, M. D.; Fleck Jr., J. A.; Steiger, A. Solution of the Schrödinger Equation by a Spectral Method. *J. Comp. Phys.* **1982**, *47*, 412–433.
- (41) Neuhauser, D.; Baer, M. The Application of Wave Packets to Reactive Atom-Diatom Systems: A New Approach. *J. Chem. Phys.* **1989**, *91*, 4651–4657.
- (42) Świderek, K.; Paneth, P. Binding Isotope Effects. *Chem. Rev.* **2013**, *113*, 7851–7879.

- (43) Wigner, E. P. On the Quantum Correction for Thermodynamic Equilibrium. *Phys. Rev.* **1932**, *40*, 749–759.
- (44) Landau, L. D.; Lifshitz, E. M. *Quantum Mechanics*; Butterworth-Heinemann: Oxford, UK, 1999.
- (45) Tannor, D. J.; Weeks, D. E. Wave Packet Correlation-Function Formulation of Scattering Theory – The Quantum Analog of Classical S-matrix Theory. *J. Chem. Phys.* **1993**, *98*, 3884–3893.
- (46) Towns, J.; Cockerill, T.; Dahan, M.; Foster, I.; Gaither, K.; Grimshaw, A.; Hazelwood, V.; Lathrop, S.; Lifka, D.; Peterson, G. D.; Roskies, R.; Scott, J.; Wilkins-Diehr, N. XSEDE: Accelerating Scientific Discovery. *Comput. Sci. Eng.* **2014**, *16*, 62–74.

# Graphical TOC Entry

